Received: 16 September 2024 | Accepted: 14 February 2025

DOI: 10.1111/1365-2478.70006

Geophysical Prospecting EAGE EUROPEAN ASSOCIATION OF GEOSCIENTISTS & ENGINEERS

ORIGINAL ARTICLE

# Sensitivity analysis with a 3D mixed-dimensional code for direct current geoelectrical investigations of landfills: synthetic tests

**Lorenzo Panzeri**[1] | **Alessio Fumagalli**[2] | **Laura Longoni**[1] | **Monica Papini**[1] | **Diego Arosio**[3]

[1]Dipartimento di Ingegneria Civile e Ambientale, Politecnico di Milano, Milan, Italy

[2]Dipartimento di Matematica, Poiltecnico di Milano, Milan, Italy

[3]Dipartimento di Scienze Chimiche e Geologiche, Università degli Studi di Modena e Reggio Emilia, Modena, Italy

**Correspondence**
Alessio Fumagalli, Politecnico di Milano.
Email: alessio.fumagalli@polimi.it

**Funding information**
Italian Minister of University and Research

## Abstract

Electrical resistivity tomography is a suitable technique for non-invasive monitoring of municipal solid waste landfills, but accurate sensitivity analysis is necessary to evaluate the effectiveness and reliability of geoelectrical investigations and to properly design data acquisition. Typically, a thin high-resistivity membrane is placed underneath the waste to prevent leakage of leachate. In the construction of a numerical framework for sensitivity computation, taking into account the actual dimensions of the electrodes and, in particular, of the membrane, can lead to extremely high computational costs. In this work, we present a novel approach for numerically computing sensitivity effectively by adopting a mixed-dimensional framework, where the membrane is approximated as a two-dimensional object and the electrodes as one-dimensional objects. The code is first validated against analytical expressions for simple four-electrode arrays and a homogeneous medium. Then it is tested in simplified landfill models, where a two-dimensional box-shaped liner separates the landfill body from the surrounding media, and 48 electrodes are used. The results show that electrodes arranged linearly along both sides of the perimeter edges of the box-shaped liner are promising for detecting liner damage, with sensitivity increasing by 2 to 3 orders of magnitude, even for damage as small as one-sixth of the electrode spacing in diameter. Good results are also obtained when simulating an electrical connection between the landfill and the surrounding media that is not due to liner damage. The configurations with the highest sensitivity directly beneath the liner are quadrupoles in which both the current and voltage dipoles have one electrode inside the liner and one electrode outside, and a two-dimensional arrangement of the electrodes. The modelled sensitivity values beneath the liner are close to a minimum sensitivity threshold derived from arbitrary and simplified assumptions. We believe that direct current surveys have the potential to detect liner damage using electrode spreads positioned along the liner perimeter, both inside and outside the landfill. However, down-scaled laboratory tests will be necessary to validate the modelling results and confirm whether the computed sensitivity values are sufficiently high to reliably detect liner damage.

KEYWORDS
computing aspects, mathematical formulation, modelling, monitoring, numerical study, resistivity

## INTRODUCTION

Today, the creation of new municipal solid waste landfills (MSWLFs) is discouraged in favour of a circular economy, with minimum and maximum rates for recycling and landfilling, respectively, established by regulatory agencies, especially in developed countries (European Commission, 2015). As a consequence, municipal solid waste landfilling is also declining, due to advances made in recycling, composting, incineration and energy recovery technologies (Nanda & Berruti, 2021). However, it is estimated that there are hundreds of thousands of active and closed landfills in the European Union (Jones et al., 2013; Wagner & Raymond, 2015) as well as in the USA and Canada (Giroux, 2014; Peters, 2016).

In recent MSWLFs, in addition to facilities for collecting leachate and gas produced by waste degradation, one or more high-density polyethylene (HDPE) liners are placed underneath the waste body to prevent leachate leakage in the subsurface and potential groundwater contamination (Nanda & Berruti, 2021). Monitoring the conditions of the liners and the materials beneath the waste is crucial in landfill management to avoid serious environmental concerns.

Direct current (DC) geoelectrical surveys are well suited to investigate the electrical resistivity of the media and can be effective in MSWLF monitoring, as the plastic liner is highly resistive and leachate is very conductive because of its high salt content. Both electrical resistivity tomography (ERT) and induced polarization have been employed for non-invasive assessment and monitoring of landfills in field (Dahlin et al., 2010; De Carlo et al., 2013; De Donno & Cardarelli, 2017; Tsourlos et al., 2014), laboratory and numerical studies (Aguzzoli et al., 2020; Binley & Daily, 2003; Frangos, 1997; Ling et al., 2019; Panzeri, Fumagalli, Zanzi, et al., 2023).

ERT investigations are typically conducted using multi-electrode resistivity meters capable of automatically performing measurements with several quadrupoles. In addition to the signal-to-noise ratio, the geometry of the quadrupole controls the depth of the investigation and spatial resolution (Loke, 2022) and can be modified to tailor the sensitivity of geoelectrical measurements to specific subsurface features or target depths. Integrating data from multiple quadrupoles helps to improve the accuracy of the resulting resistivity images and thus offers enhanced imaging capabilities of subsurface structures.

However, considering the large size of the landfills and the fact that the electrodes are generally placed around or above the waste body, the depth of investigation and the spatial resolution of the geoelectrical technique can be very limited where they are most needed, namely below the waste mass. It is well known that the sensitivity of the resistivity investigation rapidly decays away from the deployed electrodes (Loke, 2022).

In this work, we consider the sensitivity of ERT within the framework of a three-dimensional (3D) mixed-dimensional numerical model developed for MSWLF monitoring to reduce computational costs and address the ill-posedness of the geoelectrical inverse problem (Fumagalli et al., 2024). The paper is organized as follows: in the second section , we review the mixed-dimensional mathematical model, where the electrodes and the HDPE liner are modelled as one- and two-dimensional elements, respectively. In the third section , we first introduce the classical equations of geoelectrical sensitivity and then extend them to the newly developed mixed-dimensional framework. The fourth section describes some practical implementation aspects of the code used to calculate the sensitivity. The fifth section presents numerical experiments, where the sensitivity is first computed for validation purposes and then in the presence of simplified landfill models. The results of the numerical experiments are discussed in the sixth section . Finally, conclusions are drawn in the last section .

The ultimate goal of our work is to provide a tool for computing DC sensitivity and evaluating the effectiveness of geoelectrical investigations of MSWLFs. We aim to contribute to the advancement of non-destructive techniques for assessing the condition of HDPE liners and potential contaminant plumes at MSWLF sites, with implications for enhanced environmental protection and sustainable waste management practices.

## THE MATHEMATICAL MODEL

We adopt the mixed-dimensional model proposed by Fumagalli et al. (2024). In this section, for completeness, we recall the main points and equations that are useful for the derivation of the sensitivity presented in the Sensitivity section.

We indicate the domain in which the geoelectric equations will be applied, as $\Upsilon \subset \mathbb{R}^3$, with boundary $\partial\Upsilon$ and outward unit normal $\boldsymbol{n}_\partial$. We consider the following main variables: $\boldsymbol{J}_\Upsilon : \Upsilon \to \mathbb{R}^3$, the current density in [A m$^{-2}$], and $\varphi_\Upsilon : \Upsilon \to \mathbb{R}$, the electric potential in [V]. We indicate with $\boldsymbol{x} = (x_0, x_1, x_2)$ a generic point. We specify that all functions and variables hereafter depend on the spatial coordinate

$\boldsymbol{x}$, but for better readability, this dependency is omitted in the equations.

The constitutive relation between the current density $\boldsymbol{J}_\Upsilon$ and the electric potential $\varphi_\Upsilon$ is given by Ohm's law as follows:

$$\rho_\Upsilon \boldsymbol{J}_\Upsilon + \nabla\varphi_\Upsilon = \boldsymbol{0}, \tag{1}$$

where $\rho_\Upsilon$ is the electrical resistivity in [Ωm]. Gauss' law, or charge conservation equation for $\boldsymbol{J}_\Upsilon$, can be expressed as

$$\nabla \cdot \boldsymbol{J}_\Upsilon = q_\Upsilon, \tag{2}$$

with $q_\Upsilon : \Upsilon \to \mathbb{R}$ being the source of volumetric charge density in [A m$^{-3}$].

In the considered examples, $\Upsilon$ is the domain defined as $\Upsilon = \mathbb{R} \times \mathbb{R} \times \mathbb{T}$, where $\mathbb{T}$ is the hypograph of a smooth function $x_2 = t(x_0, x_1)$ representing the elevation associated with a digital terrain model, so $\mathbb{T} = \text{hyp}(t)$. For a flat terrain, we have $x_2 = \overline{x}_2$, with $\overline{x}_2 \in \mathbb{R}$, and thus we get $\mathbb{T} = (-\infty, \overline{x}_2)$ and so $\Upsilon = \mathbb{R} \times \mathbb{R} \times (-\infty, \overline{x}_2)$. However, this might be unpractical since unbounded domains are complicated to consider in numerical simulations. We know that if $q_\Upsilon$ has limited support, then it can be shown that

$$\lim_{\|\boldsymbol{x}\| \to \infty} \varphi_\Upsilon(\boldsymbol{x}) = 0 \tag{3}$$

and, with a reasonable approximation, we restrict $\Upsilon$ to be a bounded domain and impose that at its lateral and bottom boundaries the electric potential is null. On the top boundary, we have air that, for our purposes, does not interact with $\Upsilon$ and we can assume $\boldsymbol{J}_\Upsilon \cdot \boldsymbol{n}_\partial = 0$ on the top. We decompose $\partial\Upsilon$ into two non-overlapping parts $\partial^t\Upsilon$ and $\partial^o\Upsilon$, representing the top boundary (i.e., the digital terrain model) and the lateral and bottom boundaries, respectively.

By combining (1) and (2), the direct current problem can be written as: find $(\boldsymbol{J}_\Upsilon, \varphi_\Upsilon)$ in $\Upsilon$ such that

$$\begin{array}{ll} \rho_\Upsilon \boldsymbol{J}_\Upsilon + \nabla\varphi_\Upsilon = \boldsymbol{0} & \\ \nabla \cdot \boldsymbol{J}_\Upsilon = q_\Upsilon & \text{in } \Upsilon \end{array} \qquad \begin{array}{ll} \varphi_\Upsilon = 0 & \text{on } \partial^o\Upsilon \\ \boldsymbol{J}_\Upsilon \cdot \boldsymbol{n}_\partial = 0 & \text{on } \partial^t\Upsilon. \end{array} \tag{4}$$

The previous problem can be written in its primal formulation, setting $\sigma_\Upsilon = \rho_\Upsilon^{-1}$ the electric conductivity in [S m$^{-1}$] and, by substituting Ohm's law into we obtain the conservation equation, we get

$$\nabla \cdot (-\sigma_\Upsilon \nabla\varphi_\Upsilon) = q_\Upsilon \quad \text{in } \Upsilon \qquad \begin{array}{ll} \varphi_\Upsilon = 0 & \text{on } \partial^o\Upsilon \\ -\sigma_\Upsilon \nabla\varphi_\Upsilon \cdot \boldsymbol{n}_\partial = 0 & \text{on } \partial^t\Upsilon \end{array}. \tag{5}$$

It is possible to compute the solution $\varphi_\Upsilon$ at a point $\boldsymbol{y}$, by using the Green's function $g_\Upsilon^{\boldsymbol{y}}$, in [Ω], related to the point $\boldsymbol{y}$. The Green's function solves the following problem and is such that

$$\nabla \cdot (-\sigma_\Upsilon \nabla g_\Upsilon^{\boldsymbol{y}}) = \delta^{\boldsymbol{y}} \quad \Rightarrow \quad \varphi_\Upsilon(\boldsymbol{y}) = \int_\Upsilon q_\Upsilon g_\Upsilon^{\boldsymbol{y}}, \tag{6}$$

where $\delta^{\boldsymbol{y}}$ is a point Dirac delta centred at $\boldsymbol{y}$ measured in [m$^{-3}$], and the integral in (6) is a three-dimensional (3D) integral. The Green's function is a fundamental tool in solving problems related to potential theory and electrostatics. It represents the potential due to a unit point charge located at the point $\boldsymbol{y} \in \Upsilon$ and, if $\Upsilon$ is unbounded, is such that

$$\lim_{\|\boldsymbol{x}\| \to \infty} g_\Upsilon^{\boldsymbol{y}}(\boldsymbol{x}) = 0. \tag{7}$$

For a homogeneous 3D half space, electrodes at the surface and unitary injected current, the analytical expression for $g_\Upsilon^{\boldsymbol{y}}$ is well known

$$g_\Upsilon^{\boldsymbol{y}}(\boldsymbol{x}) = \frac{\rho_\Upsilon}{2\pi\|\boldsymbol{x} - \boldsymbol{y}\|}, \tag{8}$$

In contrast, except in a few cases (Sheriff et al., 1990), the Green's function has to be approximated when the half space is not homogeneous.

In municipal solid waste landfills (MSWLFs) geoelectrical investigations, the electrodes used to inject current and measure potential difference can generally be approximated as cylinders whose radius is much smaller than their height. Moreover, the low-permeability high-density polyethylene (HDPE) liner (hereafter referred to as $\lambda$) used to seal the waste body has a thickness ($\epsilon$) of a few millimetres and covers an area of thousands of square metres. Accordingly, it is numerically impractical to represent these objects with a 3D computational grid, so we follow the strategy proposed by Fumagalli et al. (2024) and approximate them as lower dimensional objects: the electrodes are represented as one-dimensional (1D) and the liner as a two-dimensional object. The grid now does not resolve either the radius of the electrodes or the thickness of the liner and can be coarsened for computational efficiency.

However, this approach requires one to consider dedicated mathematical models. More in detail, for a single electrode $\gamma$, the equations to compute $\boldsymbol{J}_\gamma$ and $\varphi_\gamma$, now expressed in [A] and [V], are summarized as: find $(j_\gamma, \boldsymbol{J}_\gamma, \varphi_\gamma)$ in $\gamma$ such that

$$\begin{array}{ll} \rho_\gamma \boldsymbol{J}_\gamma + \pi r^2 \nabla\varphi_\gamma = \boldsymbol{0} & \\ \nabla \cdot \boldsymbol{J}_\gamma - j_\gamma = 0 & \text{in } \gamma \end{array} \qquad \begin{array}{ll} \boldsymbol{J}_\gamma \cdot \boldsymbol{n}_\partial = 0 & \text{on } \partial^o\gamma \\ \boldsymbol{J}_\gamma \cdot \boldsymbol{n}_\partial = \pi r^2 \overline{J} & \text{on } \partial^t\gamma, \\ \rho_\gamma j_\gamma + \varphi_\gamma - \varphi_\Upsilon = 0 & \text{on } \gamma \end{array} \tag{9}$$

where $j_\gamma$ in [A m$^{-1}$] is the current density exchanged between the electrode and the surrounding domain $\Upsilon$ and $\rho_\gamma$ in [Ωm] is

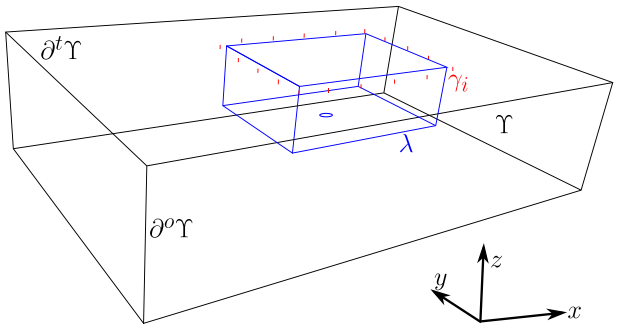


**FIGURE 1** Graphical example of a domain $\Upsilon$ with multiple electrodes $\gamma_i$ around a box-shaped liner $\lambda$. A hole in the bottom surface of the liner is also depicted. $\partial^t\Upsilon$ indicates the top boundary of the domain, while $\partial^o\Upsilon$ refers to the lateral and bottom boundaries.

the resistivity of the electrode. The top boundary of the electrode $\partial^t\gamma$ is in contact with the top boundary of the domain $\partial^t\Upsilon$, while $\partial^o\gamma$ is the portion of the electrode boundary immersed into $\Upsilon$ (Figure 1).

Having assumed the 1D representation of a cylindrical electrode $\gamma$, in (9) it can be seen that Ohm's low in (1) is now averaged over each cross section of radius $r$.

The source term $q_\Upsilon$ introduced in (4) is now given by $q_\Upsilon = -j_\gamma \delta_\gamma$, where $\delta_\gamma$ in $[\mathrm{m}^{-2}]$ is a linear delta function distributed along $\gamma$. This couples problems (4) and (9), $j_\gamma$ being the coupling variable. Moreover, the boundary condition in (9) on $\partial^o\gamma$ is the tip condition (no current flow) at the point immersed in $\Upsilon$, while on $\partial^t\gamma$ we impose the injected current $\overline{J}$, measured in $[\mathrm{A\ m}^{-2}]$.

Also for the liner $\lambda$ (Figure 1), represented as a two-dimensional object, we need a dedicated model to compute $\boldsymbol{J}_\lambda$ in $[\mathrm{A\ m}^{-1}]$ and $\varphi_\lambda$ in [V]. Thus, we consider the following problem summarized as: find $(j_\lambda, \boldsymbol{J}_\lambda, \varphi_\lambda)$ in $\lambda$ such that

$$\begin{aligned} &\rho_\lambda \boldsymbol{J}_\lambda + \epsilon \nabla \varphi_\lambda = \boldsymbol{0} && \boldsymbol{J}_\lambda \cdot \boldsymbol{n}_\partial = 0 && \text{on } \partial\lambda \\ &\qquad\qquad \text{in } \lambda \\ &\nabla \cdot \boldsymbol{J}_\lambda - j_\lambda = 0 && \epsilon\rho_\lambda j_\lambda + \varphi_\lambda - \varphi_\Upsilon = 0 && \text{on } \lambda, \end{aligned} \tag{10}$$

where $j_\lambda$ in $[\mathrm{A\ m}^{-2}]$ and $\rho_\lambda$ in $[\Omega\mathrm{m}]$ are the current density exchanged between the liner and its surrounding and the resistivity of the membrane, respectively.

In (10), it has been assumed that the liner has a thickness much smaller than its other dimensions, and so the equations were integrated along every cross section of thickness $\epsilon$. It is also assumed that the boundary of the liner $\partial\lambda$ does not exchange any current density with the surrounding. (See Figure 2 as an example of a realistic geometry, also used in the numerical examples of the Sensitivity Synthetic Tests section with multiple electrodes and a perforated liner, these are represented as lower dimensional objects.)

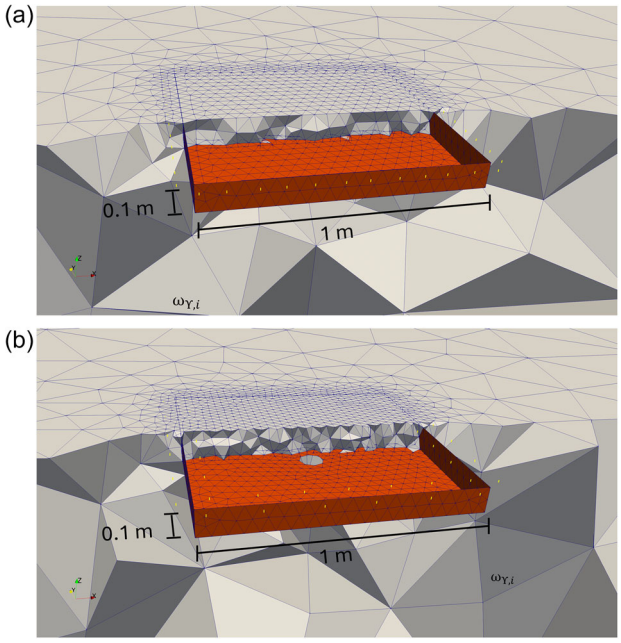


**FIGURE 2** Examples of computational grids for the mixed-dimensional model: 3D tetrahedral elements in grey, 2D triangular elements of the liner in red and 1D electrodes in yellow. (a) Forty-eight electrodes around the box-shaped liner; (b) 24 electrodes outside the liner and 24 electrodes inside, a hole in the bottom surface of the liner with its vertical walls not in contact with the top boundary of the domain. The liner has dimensions of 1 m × 1 m × 0.1 m. $\omega_{\Upsilon,i}$ indicates the generic 3D cell in the domain $\Upsilon$.

## SENSITIVITY

In geoelectrical sounding, the sensitivity is just a measure of how much the electric potential (i.e., the observed data) changes in response to a change in resistivity (i.e., the model parameters) within the considered domain. In other words, the sensitivity is fully described by the Jacobian matrix containing the first derivatives of the potential with respect to the resistivities of the model. Here, sensitivity analysis is performed through the use of Green's functions, as mentioned in Mcgillivray and Oldenburg (1990) and Park and Van (1991). In the next two subsections, we first recall the computation of sensitivity in a standard equidimensional model and then apply the same approach to our mixed-dimensional model.

### Equidimensional sensitivity

Let us consider (4) with $q_\Upsilon = I\delta^{\boldsymbol{x}}$, which represents an electrode $\gamma$ placed in position $\boldsymbol{x}$ and with $I$ the current exchanged. Consequently, in (9) we have $I = j_\gamma$.

Following the discussion in Mcgillivray and Oldenburg (1990), we assume that $\Upsilon$ can be divided into $N$ non-overlapping subdomains $\omega_{\Upsilon,i}$, which are the three-

dimensional (3D) cells of the model and will form the computational grid. We can express the resistivity, and similarly the electric conductivity, and its derivative as

$$\rho_\Upsilon(\boldsymbol{x}) = \sum_{k=1}^{N} \rho_{\Upsilon,k}\chi_{\Upsilon,k}(\boldsymbol{x}) \quad \text{and} \quad \partial_{\rho_{\Upsilon,i}}\rho_\Upsilon(\boldsymbol{x}) = \chi_{\Upsilon,i}(\boldsymbol{x}), \tag{11}$$

where $\partial_{\rho_{\Upsilon,i}}\star = \frac{\partial\star}{\partial\rho_{\Upsilon,i}}$ for brevity and $\chi_{\Upsilon,i}$ is the dimensionless indication function of the $i$th subdomain defined as

$$\chi_{\Upsilon,i}(\boldsymbol{x}) = \begin{cases} 1 & \text{if } \boldsymbol{x} \in \omega_{\Upsilon,i} \\ 0 & \text{otherwise} \end{cases}. \tag{12}$$

Since both variables depend on the resistivity of the system $\boldsymbol{J}_\Upsilon = \boldsymbol{J}_\Upsilon(\rho_\Upsilon)$ and $\varphi_\Upsilon = \varphi_\Upsilon(\rho_\Upsilon)$, we define the sensitivity associated with the resistivity in the subdomain $\omega_{\Upsilon,i}$ as

$$\boldsymbol{J}_{\Upsilon,i} = \partial_{\rho_{\Upsilon,i}}\boldsymbol{J}_\Upsilon \quad \text{and} \quad \varphi_{\Upsilon,i} = \partial_{\rho_{\Upsilon,i}}\varphi_\Upsilon \tag{13}$$

with dimensions [A S $m^{-3}$] and [V S $m^{-1}$] = [A $m^{-1}$], respectively. We now differentiate the first equation of (4) to get the following expression:

$$\begin{aligned} \partial_{\rho_{\Upsilon,i}}(\rho_\Upsilon\boldsymbol{J}_\Upsilon + \nabla\varphi_\Upsilon) &= \chi_{\Upsilon,i}\boldsymbol{J}_\Upsilon + \rho_\Upsilon\boldsymbol{J}_{\Upsilon,i} + \nabla(\partial_{\rho_{\Upsilon,i}}\varphi_\Upsilon) \\ &= \chi_{\Upsilon,i}\boldsymbol{J}_\Upsilon + \rho_\Upsilon\boldsymbol{J}_{\Upsilon,i} + \nabla\varphi_{\Upsilon,i} = \boldsymbol{0} \end{aligned} \tag{14}$$

while the second equation of (4) becomes

$$\partial_{\rho_{\Upsilon,i}}\nabla\cdot\boldsymbol{J}_\Upsilon = \partial_{\rho_{\Upsilon,i}}(I\delta^{\boldsymbol{x}}) \quad \Rightarrow \quad \nabla\cdot\boldsymbol{J}_{\Upsilon,i} = 0. \tag{15}$$

Thus, the system for computing the sensitivity of the current density and the electric potential is given by finding $(\boldsymbol{J}_{\Upsilon,i}, \varphi_{\Upsilon,i})$ such that

$$\begin{cases} \rho_\Upsilon\boldsymbol{J}_{\Upsilon,i} + \nabla\varphi_{\Upsilon,i} = -\chi_{\Upsilon,i}\boldsymbol{J}_\Upsilon \\ \nabla\cdot\boldsymbol{J}_{\Upsilon,i} = 0 \end{cases} \quad \text{in } \Upsilon. \tag{16}$$

The above equations correspond to equation (70a) in Mcgillivray and Oldenburg (1990) and can also be written in the primal formulation (by substituting the first equation into the second)

$$\nabla\cdot(-\sigma_\Upsilon\nabla\varphi_{\Upsilon,i}) = \nabla\cdot(\chi_{\Upsilon,i}\sigma_\Upsilon\boldsymbol{J}_\Upsilon). \tag{17}$$

We suppose that a second electrode is used to measure the electric potential at the point $\boldsymbol{y}$, thus we need to compute the sensitivity not in all the domains but only in correspondence to that electrode. To keep the notation simple, we use subscripts to indicate that all the forthcoming integrals in this section are 3D integrals over $\Upsilon$ or $\omega_{\Upsilon,i}$. We get that, by considering (6) now applied to $\varphi_{\Upsilon,i}$, the expression is

$$\begin{aligned} \varphi_{\Upsilon,i}(\boldsymbol{y}) &= \int_\Upsilon \nabla\cdot(\chi_{\Upsilon,i}\sigma_\Upsilon\boldsymbol{J}_\Upsilon)g_\Upsilon^{\boldsymbol{y}} = -\int_\Upsilon \chi_{\Upsilon,i}\sigma_\Upsilon\boldsymbol{J}_\Upsilon\cdot\nabla g_\Upsilon^{\boldsymbol{y}} \\ &= \sigma_{\Upsilon,i}^2\int_{\omega_{\Upsilon,i}} \nabla\varphi_\Upsilon\cdot\nabla g_\Upsilon^{\boldsymbol{y}} = I\sigma_{\Upsilon,i}^2\int_{\omega_{\Upsilon,i}} \nabla g_\Upsilon^{\boldsymbol{x}}\cdot\nabla g_\Upsilon^{\boldsymbol{y}}, \end{aligned} \tag{18}$$

which is the 3D version of equation (73) in Mcgillivray and Oldenburg (1990) and represents an easy way to compute the sensitivity of the $i$th subdomain, measured at the observation point located in $\boldsymbol{y}$, since $\overline{\boldsymbol{J}}$ is set in (9) and the previous expression depends only on the computation of the Green's functions associated with the two electrodes. In other terms, (18) is the relation to compute the sensitivity of a pole–pole configuration. We point out that (18) shows that the sensitivity depends linearly on the injected current and has dimension [A $m^{-1}$] in agreement with Mcgillivray and Oldenburg (1990).

Now, let us consider the case of a quadrupole, where two electrodes are used to circulate the current density, while the other two measure the difference in electric potential. One of the current electrodes is used to inject the current density at the point $\boldsymbol{x}_0$, while the other one extracts the same amount at the point $\boldsymbol{x}_1$, clearly being $\boldsymbol{x}_0 \neq \boldsymbol{x}_1$. Calculating the electric potential requires setting $q_\Upsilon = I(\delta^{\boldsymbol{x}_0} - \delta^{\boldsymbol{x}_1})$ in (4). The computation of the sensitivity is now associated with the difference of $\varphi_\Upsilon$ at the two measuring electrodes at position $\boldsymbol{y}_0$ and $\boldsymbol{y}_1$, with $\boldsymbol{y}_0 \neq \boldsymbol{y}_1$. We have

$$\begin{aligned} &\varphi_{\Upsilon,i}(\boldsymbol{y}_0) - \varphi_{\Upsilon,i}(\boldsymbol{y}_1) \\ &= -\int_\Upsilon \chi_{\Upsilon,i}\sigma_\Upsilon\boldsymbol{J}_\Upsilon\cdot\nabla g_\Upsilon^{\boldsymbol{y}_0} + \int_\Upsilon \chi_{\Upsilon,i}\sigma_\Upsilon\boldsymbol{J}_\Upsilon\cdot\nabla g_\Upsilon^{\boldsymbol{y}_1} \\ &= \sigma_{\Upsilon,i}^2\int_{\omega_{\Upsilon,i}} \nabla\varphi_\Upsilon\cdot\nabla g_\Upsilon^{\boldsymbol{y}_0} - \sigma_{\Upsilon,i}^2\int_{\omega_{\Upsilon,i}} \nabla\varphi_\Upsilon\cdot\nabla g_\Upsilon^{\boldsymbol{y}_1} \end{aligned} \tag{19}$$

since $\varphi_\Upsilon$ is computed with two delta functions, we can use again the Green's functions to express it as $\varphi_\Upsilon = I(g_\Upsilon^{\boldsymbol{x}_0} - g_\Upsilon^{\boldsymbol{x}_1})$ and thus the sensitivity can be computed as linear combinations of pole–pole sensitivity functions (18) as

$$\begin{aligned} &\varphi_{\Upsilon,i}(\boldsymbol{y}_0) - \varphi_{\Upsilon,i}(\boldsymbol{y}_1) \\ &= +I\sigma_{\Upsilon,i}^2\int_{\omega_{\Upsilon,i}} \nabla g_\Upsilon^{\boldsymbol{x}_0}\cdot\nabla g_\Upsilon^{\boldsymbol{y}_0} - I\sigma_{\Upsilon,i}^2\int_{\omega_{\Upsilon,i}} \nabla g_\Upsilon^{\boldsymbol{x}_1}\cdot\nabla g_\Upsilon^{\boldsymbol{y}_0} \\ &- I\sigma_{\Upsilon,i}^2\int_{\omega_{\Upsilon,i}} \nabla g_\Upsilon^{\boldsymbol{x}_0}\cdot\nabla g_\Upsilon^{\boldsymbol{y}_1} + I\sigma_{\Upsilon,i}^2\int_{\omega_{\Upsilon,i}} \nabla g_\Upsilon^{\boldsymbol{x}_1}\cdot\nabla g_\Upsilon^{\boldsymbol{y}_1}. \end{aligned} \tag{20}$$

In the case of multiple electrode configurations, a simple way to obtain the (approximate) global sensitivity is to sum the absolute values of the sensitivities associated with each configuration (Loke, 2022).

## Mixed-dimensional sensitivity

Due to the presence of the liner, we need to consider the computation of the sensitivity in the mixed-dimensional framework. As in the previous section, in (4) we set $q_\Upsilon = I\delta^{\boldsymbol{x}}$ and also consider (10) to describe the liner. In addition to the sensitivity associated with the variables in the 3D domain $\Upsilon$ expressed in (13), we need to also consider the followings associated with the liner

$$j_{\lambda,i} = \partial_{\rho_{\lambda,i}} j_\lambda \quad \text{and} \quad \boldsymbol{J}_{\lambda,i} = \partial_{\rho_{\lambda,i}} \boldsymbol{J}_\lambda \quad \text{and} \quad \varphi_{\lambda,i} = \partial_{\rho_{\lambda,i}} \varphi_\lambda. \tag{21}$$

The sensitivities have dimensions [A S m$^{-3}$], [A S m$^{-2}$] and [V S m$^{-1}$] = [A m$^{-1}$], respectively. Given the partitioning of $\lambda$, the resistivity can be written in the following way:

$$\rho_\lambda(\boldsymbol{x}) = \sum_{k=1}^{N_\lambda} \rho_{\lambda,k} \chi_{\lambda,k}(\boldsymbol{x}) \tag{22}$$

with $N_\lambda$ is the number of subdomains that make up the liner and $\chi_{\lambda,k}$ is the indication function of the $k$th subdomain $\omega_{\lambda,k}$. Let us first assume that the variation of resistivity is associated with a subdomain $\omega_{\Upsilon,i}$ that belongs to $\Upsilon$. We have

$$\begin{cases} \rho_\Upsilon \boldsymbol{J}_{\Upsilon,i} + \nabla\varphi_{\Upsilon,i} = -\chi_{\Upsilon,i}\boldsymbol{J}_\Upsilon \\ \nabla\cdot\boldsymbol{J}_{\Upsilon,i} = 0 \end{cases} \text{in } \Upsilon \qquad \begin{cases} \rho_\lambda \boldsymbol{J}_{\lambda,i} + \epsilon\nabla\varphi_{\lambda,i} = \boldsymbol{0} \\ \nabla\cdot\boldsymbol{J}_{\lambda,i} - j_{\lambda,i} = 0 \end{cases} \text{in } \lambda, \tag{23}$$

while for the interface condition, we get

$$\partial_{\rho_{\Upsilon,i}}(\epsilon\rho_\lambda j_\lambda + \varphi_\lambda - \varphi_\Upsilon) = \epsilon\rho_\lambda \partial_{\rho_{\Upsilon,i}} j_\lambda + \partial_{\rho_{\Upsilon,i}}\varphi_\lambda - \partial_{\rho_{\Upsilon,i}}\varphi_\Upsilon = \epsilon\rho_{\lambda,i} j_{\lambda,i} + \varphi_{\lambda,i} - \varphi_{\Upsilon,i} = 0. \tag{24}$$

The above set of equations can also be written in primal form as

$$\begin{cases} \nabla\cdot(-\sigma_\Upsilon\nabla\varphi_{\Upsilon,i}) = \nabla\cdot(\chi_{\Upsilon,i}\sigma_\Upsilon\boldsymbol{J}_\Upsilon) & \text{in } \Upsilon \\ \nabla\cdot(-\epsilon\sigma_\lambda\nabla\varphi_{\lambda,i}) - j_{\lambda,i} = 0 & \text{in } \lambda\,. \\ \epsilon\rho_\lambda j_{\lambda,i} + \varphi_{\lambda,i} - \varphi_{\Upsilon,i} = 0 & \text{on } \lambda \end{cases} \tag{25}$$

Let us now extend the concept of the Green's function to a mixed-dimensional framework. We call the compound $(g^{\boldsymbol{y}}_\Upsilon, g^{\boldsymbol{y}}_\lambda, w^{\boldsymbol{y}}_\lambda)$, in [Ω], [Ω], and [m$^{-2}$], respectively, the mixed-dimensional Green's function related to a point $\boldsymbol{y}$, where a measuring electrode has been placed. The above compound is the solution of the following problem:

$$\begin{cases} \nabla\cdot(-\sigma_\Upsilon\nabla g^{\boldsymbol{y}}_\Upsilon) = \delta^{\boldsymbol{y}} & \text{in } \Upsilon \\ \nabla\cdot(-\epsilon\sigma_\lambda\nabla g^{\boldsymbol{y}}_\lambda) - w^{\boldsymbol{y}}_\lambda = 0 & \text{in } \lambda \\ \epsilon\rho_\lambda w^{\boldsymbol{y}}_\lambda + g^{\boldsymbol{y}}_\lambda - g^{\boldsymbol{y}}_\Upsilon = 0 & \text{on } \lambda. \end{cases} \tag{26}$$

The representation theorem Salsa (2016) can be extended to the mixed-dimensional case and gives us the possibility to evaluate the sensitivity of the electric potential. In addition to the notation previously introduced, we point out that all the integrals over $\lambda$ or $\omega_{\lambda,i}$ are two-dimensional integrals. If $q_\lambda$ and $\varpi_\lambda$ are the source terms associated with the equation in $\lambda$ and at the interface between $\lambda$ and its surrounding, we have

$$\begin{aligned} \varphi_{\Upsilon,i}(\boldsymbol{y}) &= \int_\Upsilon q_\Upsilon g^{\boldsymbol{y}}_\Upsilon + \int_\lambda q_\lambda g^{\boldsymbol{y}}_\lambda - \int_\lambda \varpi_\lambda w^{\boldsymbol{y}}_\lambda \\ &= \int_\Upsilon \nabla\cdot(\chi_{\Upsilon,i}\sigma_\Upsilon\boldsymbol{J}_\Upsilon) g^{\boldsymbol{y}}_\Upsilon \\ &= \sigma^2_{\Upsilon,i}\int_{\omega_{\Upsilon,i}} \nabla\varphi_\Upsilon\cdot\nabla g^{\boldsymbol{y}}_\Upsilon \end{aligned} \tag{27}$$

and since $\varphi_\Upsilon$ can be expressed in terms of $Ig^{\boldsymbol{x}}_\Upsilon$, we obtain the following expression for the sensitivity:

$$\varphi_{\Upsilon,i}(\boldsymbol{y}) = I\sigma^2_{\Upsilon,i}\int_{\omega_{\Upsilon,i}} \nabla g^{\boldsymbol{x}}_\Upsilon\cdot\nabla g^{\boldsymbol{y}}_\Upsilon. \tag{28}$$

Let us assume now that the variation of the resistivity is associated with a subdomain of the liner, named $\omega_{\lambda,i} \subset \lambda$, then the equations for the sensitivity are now given by

$$\begin{cases} \rho_\Upsilon \boldsymbol{J}_{\Upsilon,i} + \nabla\varphi_{\Upsilon,i} = \boldsymbol{0} \\ \nabla\cdot\boldsymbol{J}_{\Upsilon,i} = 0 \end{cases} \text{in } \Upsilon \qquad \begin{cases} \rho_\lambda \boldsymbol{J}_{\lambda,i} + \epsilon\nabla\varphi_{\lambda,i} = -\chi_{\lambda,i}\boldsymbol{J}_\lambda \\ \nabla\cdot\boldsymbol{J}_{\lambda,i} - j_{\lambda,i} = 0 \end{cases} \text{in } \lambda, \tag{29}$$

while for the interface condition, we get

$$\begin{aligned} \partial_{\rho_{\lambda,i}}(\epsilon\rho_\lambda j_\lambda + \varphi_\lambda - \varphi_\Upsilon) &= \epsilon\chi_{\lambda,i} j_\lambda + \epsilon\rho_\lambda \partial_{\rho_i} j_\lambda + \partial_{\rho_{\lambda,i}}\varphi_\lambda - \partial_{\rho_{\partial,i}}\varphi_\Upsilon = \\ &= \epsilon\chi_{\lambda,i} j_\lambda + \epsilon\rho_\lambda j_{\lambda,i} + \varphi_{\lambda,i} - \varphi_{\Upsilon,i} = 0. \end{aligned} \tag{30}$$

The above set of equations can also be written in primal form, in terms only of $(\varphi_{\Upsilon,i}, \varphi_{\lambda,i}, j_{\lambda,i})$, as

$$\begin{cases} \nabla\cdot(-\sigma_\Upsilon\nabla\varphi_{\Upsilon,i}) = 0 & \text{in } \Upsilon \\ \nabla\cdot(-\epsilon\sigma_\lambda\nabla\varphi_{\lambda,i}) - j_{\lambda,i} = \nabla\cdot(\chi_{\lambda,i}\sigma_\lambda\boldsymbol{J}_\lambda) & \text{in } \lambda\,. \\ \epsilon\rho_\lambda j_{\lambda,i} + \varphi_{\lambda,i} - \varphi_{\Upsilon,i} = -\epsilon\chi_{\lambda,i} j_\lambda & \text{on } \lambda \end{cases} \tag{31}$$

and thus the sensitivity can be computed now with the following expression:

$$\begin{aligned}\varphi_{\Upsilon,i}(\boldsymbol{y}) &= \int_{\Upsilon} q_{\Upsilon} g^{\boldsymbol{y}}_{\Upsilon} + \int_{\lambda} q_{\lambda} g^{\boldsymbol{y}}_{\lambda} - \int_{\lambda} \varpi_{\lambda} w^{\boldsymbol{y}}_{\lambda} \\ &= \int_{\lambda} \nabla \cdot (\chi_{\lambda,i} \sigma_{\lambda} \boldsymbol{J}_{\lambda}) g^{\boldsymbol{y}}_{\lambda} + \int_{\lambda} \epsilon \chi_{\lambda,i} j_{\lambda} w^{\boldsymbol{y}}_{\lambda} \\ &= -\int_{\lambda} \chi_{\lambda,i} \sigma_{\lambda} \boldsymbol{J}_{\lambda} \cdot \nabla g^{\boldsymbol{y}}_{\lambda} + \epsilon \int_{\omega_{\lambda,i}} j_{\lambda} w^{\boldsymbol{y}}_{\lambda} \\ &= \epsilon \sigma^2_{\lambda,i} \int_{\omega_{\lambda,i}} \nabla \varphi_{\lambda} \cdot \nabla g^{\boldsymbol{y}}_{\lambda} + \epsilon \int_{\omega_{\lambda,i}} j_{\lambda} w^{\boldsymbol{y}}_{\lambda}.\end{aligned} \tag{32}$$

Finally, since $\varphi_{\lambda}$ and $j_{\lambda}$ can be expressed in terms of Green's function at $\boldsymbol{x}$, we get

$$\varphi_{\Upsilon,i}(\boldsymbol{y}) = I\epsilon\sigma^2_{\lambda,i} \int_{\omega_{\lambda,i}} \nabla g^{\boldsymbol{x}}_{\lambda} \cdot \nabla g^{\boldsymbol{y}}_{\lambda} + I\epsilon \int_{\omega_{\lambda,i}} w^{\boldsymbol{x}}_{\lambda} w^{\boldsymbol{y}}_{\lambda}. \tag{33}$$

When a quadrupole is considered, the previous expressions can be extended in a similar manner to (20).

## NUMERICAL MODEL

In this section, we discuss how to numerically approximate the computation of the sensitivity described previously. In particular, in the first subsection, we discuss the numerical scheme adopted and the strategy to couple the grid across the different dimensions. The next subsection is devoted to implementation aspects in order to speed up the computation of the sensitivity.

### Discretization

We base our discretization choices on Panzeri, Fumagalli, Aguzzoli, et al. (2023) and Fumagalli et al. (2024), and here we recall the main aspects. For a more detailed and complete discussion, refer to the aforementioned works.

For the approximation of the domain $\Upsilon$, the liner $\lambda$ and the electrodes $\gamma$, we consider the computational grids made of simplices built with Gmsh (Geuzaine & Remacle, 2009). For the numerical approximation of the problem, for each dimension, we utilize the multi-point flux approximation (MPFA) scheme (Aavatsmark, 2007, 2002), which is a finite-volume scheme where the degrees of freedom are one for each cell of the grid. MPFA solves the problem in primal form, is convergent and guarantees local conservation of the current density for each grid cell, as discussed in the aforementioned works, which is an important property for our application, particularly in the computation of the sensitivity. To compute the local gradient of the solution, we first calculate the normal component of the current density on each face and then interpolate over the lowest order Raviart–Thomas space (Raviart & Thomas, 1977).

A key aspect of the discretization is associated with the coupling between the dimensions; in particular, we consider a conforming mortar-based strategy for the coupling between the liner and the surrounding material. This means that we consider additional grids on each side of the liner, which conform to the liner grid, where the interface variables ($j_{\lambda}$ or $w_{\lambda}$) are defined. Their degrees of freedom are one per cell and represent the interface variable. The three-dimensional grid conforms to the liner grid; see an example reported in Figure 2.

To achieve coupling between the electrodes and the domain $\Upsilon$, we embed the computational grids of the electrodes into the grid cells of the domain. This is an effective strategy to reduce the number of three-dimensional cells needed for the coupling but requires a dedicated approach for the discretization of the interface law. As done before, we consider a mortar-based scheme in which a single grid is constructed conforming to the electrode grid but embedded in the three-dimensional grid. Also, in this case, we define the interface variables ($j_{\gamma}$) on the mortar grid, with one degree of freedom per cell.

Using the discretization schemes, we construct a linear system with a saddle-point structure. With an abuse of notation, we indicate the discrete unknowns with the same symbols as their continuous counterparts. The problem now reads: find $(\varphi_{\Upsilon}, \varphi_{\lambda}, \varphi_{\gamma}, j_{\lambda}, j_{\gamma})$ solution of the following linear system:

$$\begin{bmatrix} A & & & -B_{\lambda}^{\top} & -B_{\gamma}^{\top} \\ & A_{\lambda} & & -C_{\lambda}^{\top} & \\ & & A_{\gamma} & & -C_{\gamma}^{\top} \\ B_{\lambda} & C_{\lambda} & & M_{\lambda} & \\ B_{\gamma} & & C_{\gamma} & & M_{\gamma} \end{bmatrix} \begin{bmatrix} \varphi \\ \varphi_{\lambda} \\ \varphi_{\gamma} \\ j_{\lambda} \\ j_{\gamma} \end{bmatrix} = \begin{bmatrix} 0 \\ 0 \\ j_{bc} \\ 0 \\ 0 \end{bmatrix}, \tag{34}$$

where the $A$-matrices represent the stiffness matrices associated with each dimension, the $M$-matrices are mass matrices for the mortar variables, the $B$-matrices are the coupling between the mortars and the three-dimensional variables and the $C$-matrices are the coupling between the mortars and the lower dimensional variables. Finally, on the right-hand side, $j_{bc}$ represents the current density injected by the current electrodes, an approximate boundary condition of (9). The computation of the Green's functions in (26) requires the solution of a linear system where the matrix is the same as in (34), and the right-hand side term is associated with a specific potential electrode.

## Implementation aspects

The computation of the sensitivity, either for single or multiple electrodes and both for the equidimensional and the mixed-dimensional cases (see (18), (20), (28) and (33)), requires the evaluation of the Green's functions associated with the considered electrodes. Moreover, it is worth pointing out that the classical direct current problem (4) and the sensitivity analysis (16) have very similar equations and can be both expressed in terms of the Green's functions.

By exploiting this similarity, in our code, we compute the Green's functions for all the deployed electrodes, and then we simply linearly combine them to compute the voltage difference as well as the sensitivity for each considered electrode configuration. As mentioned above, for several configurations, the global sensitivity is obtained by summing the absolute values of the sensitivity for each configuration.

Another way to speed up the code is to observe that Green's functions all solve the same problem, similar to the one in (34), but with different source-term positions. This means that thanks to the chosen numerical scheme, we can assemble the discretization matrix only once and select a matrix as the right-hand side, where each column represents a unit source term associated with an electrode. By considering standard software packages, for example, SuperLU (Li, 2005), we can speed up the solution of the linear problem.

Finally, on a practical level, imposing the condition (3) may not be feasible. Therefore, we limit the computational domain and instead impose a homogeneous boundary condition on $\varphi$ to approximate the real condition (3). This approximation becomes more accurate as the computational domain increases but at the cost of greater computational effort. Since the accuracy of the electric potential is less critical far from the electrodes and liner, we coarsen the grid to achieve a more manageable computational cost.

# SENSITIVITY SYNTHETIC TESTS

The mathematical approach to the direct current problem described in the previous sections has been validated and tested by Fumagalli et al. (2024). The validation process involved comparing the solver with established analytical solutions (Aldridge & Oldenburg, 1989;Sheriff et al., 1990), other software (Rücker et al., 2017) as well as laboratory experiments (Fumagalli et al., 2024; Panzeri, Fumagalli, Aguzzoli, et al., 2023). Testing, even in very simple setups, confirmed the ability of geoelectrical surveys to detect damaged liners, paving the way for more complex investigations in real-world applications.

Following a similar approach, here we first validate our three-dimensional (3D) code for geoelectrical sensitivity analysis by considering a few common quadrupoles. Next, we conduct numerical tests in downscaled and simplified scenarios that are representative of geoelectrical investigations of landfills. Downscaling the domain does not impact computational costs because the grid cells and electrode spacing are proportionally reduced; this step is primarily intended for future comparison with laboratory tests. The domain size is carefully chosen to be large enough to avoid any boundary effects in all simulations. Accordingly, the depth is set to two times the spacing between the two furthest electrodes.

In all tests, the domain is discretized with an unstructured grid with Gmsh software (Geuzaine & Remacle, 2009) and the modelled sensitivity values are normalized by the volume of each cell. The injected current is 1 A.

## Four-electrode arrays

We consider the Wenner–alpha and dipole–dipole ($n = 1$) arrays because they are the most commonly used quadrupoles due to their versatility and effectiveness. Furthermore, and most interestingly, the Wenner array has a strong ability to detect horizontal structures, as its sensitivity exhibits a marked gradient with depth. In contrast, the dipole–dipole array is most sensitive to changes in resistivity along the horizontal direction.

For both arrays, electrodes are placed on the surface of a 3D homogeneous half-space with dimensions of 6 m × 4 m × 2 m. Assuming the origin of the reference system is at the lower bottom corner of the domain, the coordinates of the furthest electrodes are (2, 2, 2) 'm' and (4, 2, 2) 'm', respectively, with an inter-electrode distance of 0.66 m. The electrode configurations are C1-P1-P2-C2 and C2-C1-P1-P2 for Wenner–alpha and dipole–dipole arrays, respectively, being C1 and P1 positive current and potential electrodes. To obtain accurate results without excessively increasing computational costs, we set the characteristic length of the tetrahedral mesh elements to 0.05 m near the electrodes and 0.5 m near the domain boundaries. For validation purposes, we consider the analytical expression of the pole–pole sensitivity (18) described in Loke and Barker (1995).

Figure 3 shows the sensitivity values on vertical slices extracted along the tested arrays from the 3D domain. Figure 3a–c is obtained using the analytical expression evaluated on a structured grid with 0.05 m spatial sampling, while Figure 3b–d shows the modelled results. It is worth noting that the structured grids contain about 340,000 elements, compared to only 9500 elements in the unstructured grids.

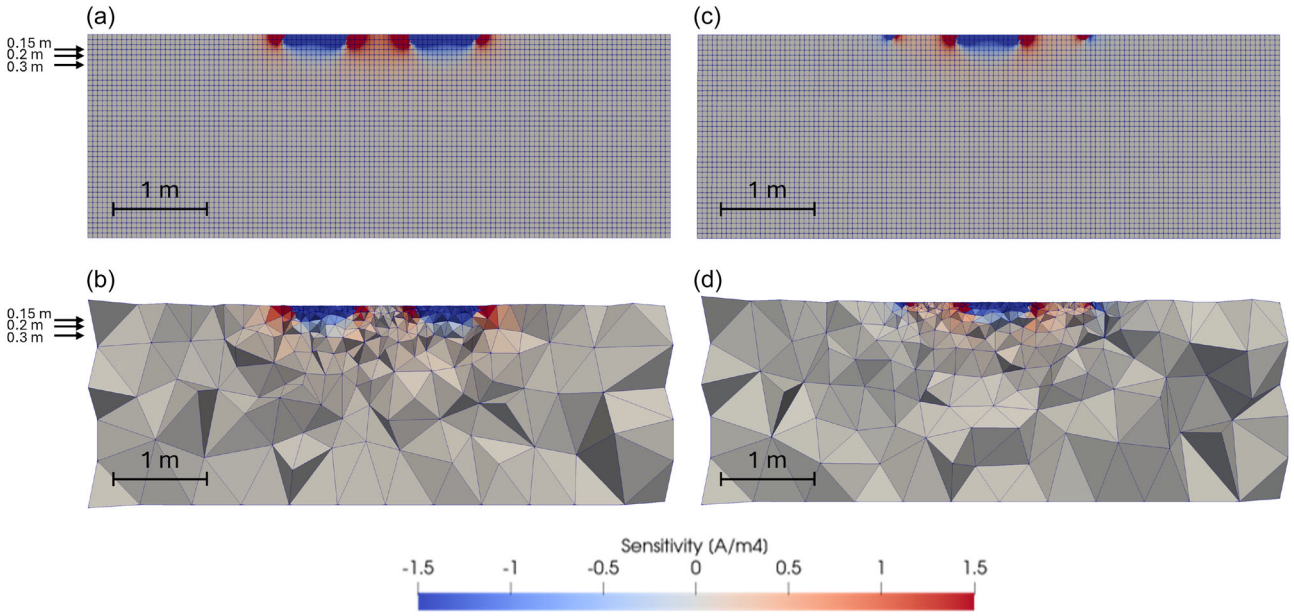


**FIGURE 3** Vertical slices of sensitivity values for Wenner–alpha (a) and (b) and dipole–dipole (c) and (d) arrays and a homogeneous half-space. (a)–(c) show plots of the analytical expression (18), while (b)–(d) show the modelled results. Both arrays have a total length of 2 m. Arrows indicate the depths at which the computed sensitivities are evaluated (see the Discussion section and Figures 6 and 7).

## Forty-eight-electrode arrays and a simplified landfill

For our downscaled tests, we set a 3D domain with dimensions $10\ \text{m} \times 10\ \text{m} \times 4\ \text{m}$, with a $1\ \text{m} \times 1\ \text{m} \times 0.1\ \text{m}$ box-shaped liner placed in the top centre (i.e., the vertical walls of the box are in contact with the top surface of the domain; see Figure 2a). Obviously, the liner is modelled as a 2D object by our mixed-dimensional code. The resistivity values inside and outside the liner (i.e., the landfill) are set to 20 and 100Ωm, respectively (Bernstone et al., 2000). The resistivity of the liner is set to $10^{15}$Ωm in agreement with the electrical properties of HDPE. The characteristic length of the computational grid is set to 0.02 m near the electrodes, to 0.05 m for the liner, and to 2 m at the boundaries of the domain (Figure 2). We assume 48 channels, as this is standard for most multi-electrode resistivitymeters on the market, deployed at the surface. In general, electrodes placed near the perimeter edges of the liner are preferable to those positioned across the landfill body because the latter, due to the elevation of the landfill, are farther from the bottom of the landfill, resulting in reduced penetration and lower resolution at depth.

Three different settings are defined: In case 1, 48 electrodes were deployed along the outer perimeter of the liner with a spacing of 0.08 m (Figure 2a); in case 2, 24 electrodes with 0.16 m spacing along the outer perimeter of the liner and 24 electrodes with 0.12 m spacing along the inner perimeter of the liner (Figure 2b); in case 3, 24 electrodes with 0.16 m spacing along the outer perimeter of the liner and 24 electrodes along a grid inside the liner (0.2 m spacing along $x$ and 0.14 m spacing along $y$). All cases involve approximately 15,000 cells and more than 635,000 configurations for the evaluation of sensitivity, considering all possible electrode combinations and permutations (excluding reciprocal configurations) with geometric factors smaller than $10^4$ m, including pole–dipole and pole–pole arrays. For all the settings, we also considered a test with a 0.1 m diameter hole in the bottom surface of the liner (Figure 2b).

Figures 4 and 5 show some images of the sensitivity computed for cases 1 and 3.

In addition, cases 2 and 3 are tested with the box-shaped liner shifted downward by 0.05 m, so its vertical walls are not in contact with the top boundary of the 3D domain (Figure 2b). This setup simulates the condition of an electrical connection between the landfill and the surrounding media that is not due to damage to the liner. The electrical connection could be caused by movements of the liner due to the weight of the waste or by materials that can accidentally cover the perimeter edges of the liner.

## DISCUSSION

As far as validation is concerned, Figures 6 and 7 report the results obtained for the Wenner–alpha and dipole–dipole arrays, respectively. More in detail, the sensitivity values computed with our code are evaluated along horizontal lines at 0.15 m, 0.2 m and 0.3 m depth below the arrays, and analytical values are computed at the same positions (see arrows in Figure 3a,b) with (18), as mentioned in the previous

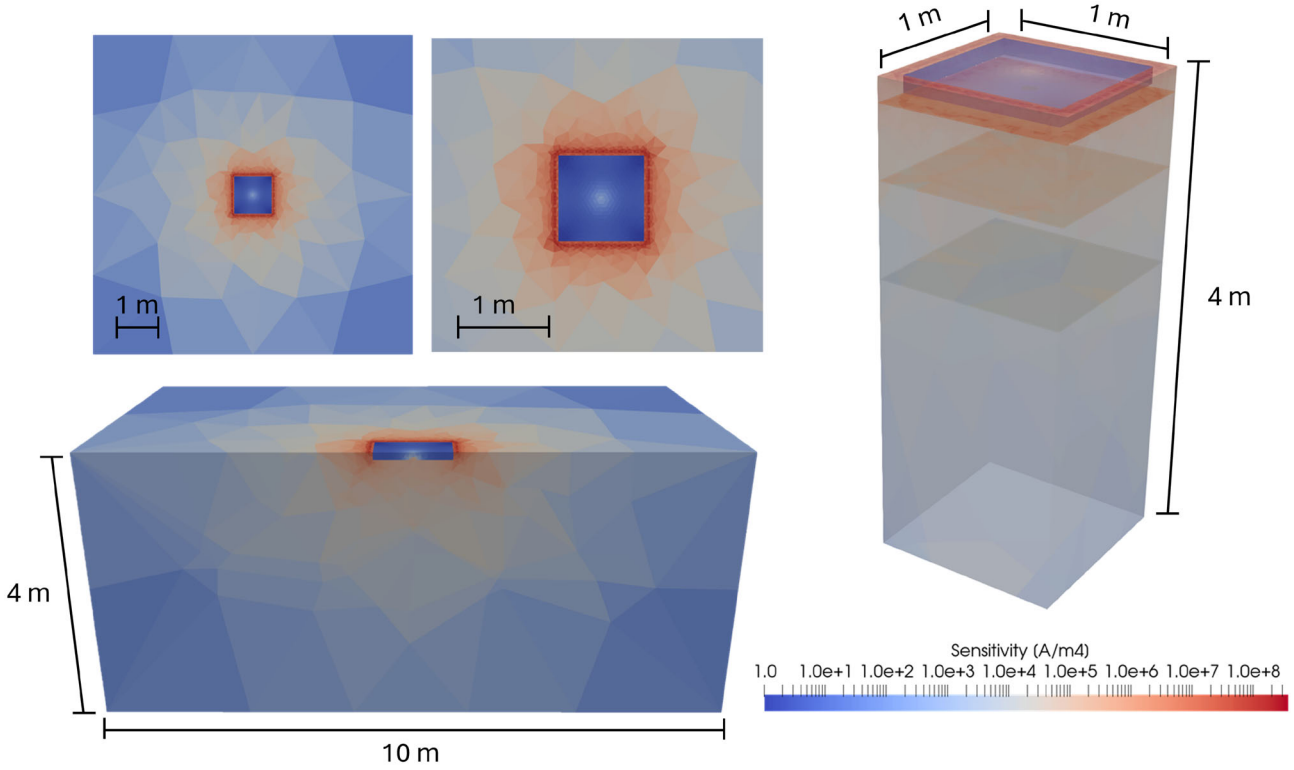


**FIGURE 4** Images of computed sensitivity for case 1 with a 0.1 m diameter hole in the bottom surface of the liner. From top-left, clockwise: top view, zoomed top view, volume below the box-shaped liner with three depth slices, vertical cut. (See text for details.)

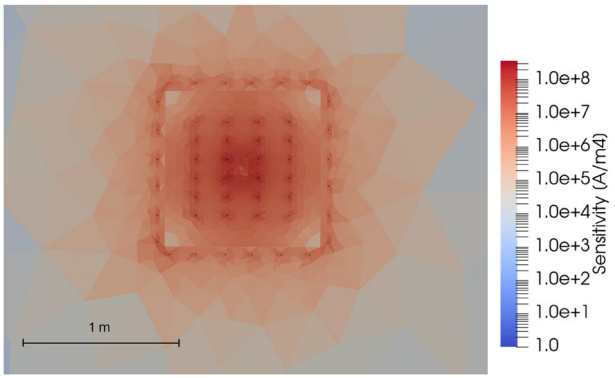


**FIGURE 5** Zoomed top view of the computed sensitivity for case 3 with a hole in the middle of the liner.

paragraph. The irregular stairstep plots are due to the different sizes of the mesh elements intercepted by the horizontal lines (see Figure 3b–d).

We can observe a very good match between the simulated and analytical values, with the per cent root mean square error (RMSE) around 8% and 4% at 0.15 m depth for Wenner–alpha and dipole–dipole arrays, respectively. As expected, peaks are recorded near the electrodes at shallow depths (see, e.g., Mcgillivray & Oldenburg, 1990). By considering even shallower depths, the amplitude of the peaks increases, and the mismatch between modelled and analytical values tends to grow because of the difficulty of the numerical code in handling the singularity of the solution at a reasonable computational cost. In contrast, the per cent RMSE is below 1% at a depth of 0.3 m. At this depth (approximately half the electrode spacing), a significant decrease in sensitivity is observed throughout the domain, consistent with the median depth of investigation (Edwards, 1977), which is approximately 15% of the total length for both arrays (Loke, 2022). The plots also indicate a higher vertical sensitivity gradient for the Wenner–alpha array, related to its high vertical resolution. In contrast, the pronounced lateral sensitivity gradients of the dipole–dipole array confirm its good horizontal resolution.

Regarding the results obtained from the simplified landfill setups, we first note that the results of case 3 do not differ significantly from those of case 2; therefore, they will not be discussed further. Second, we note that computing the global sensitivity as the sum of the absolute values of the sensitivities associated with each configuration is a simple but rough method because it does not account for the fact that information from two measurements of the same region might not be independent. A more mathematically rigorous (and computationally intensive) approach would involve, for example, considering the model resolution matrix, which relates the estimated resistivity values to the actual values in the geoelectrical inverse problem (Day-Lewis & Binley, 2005).

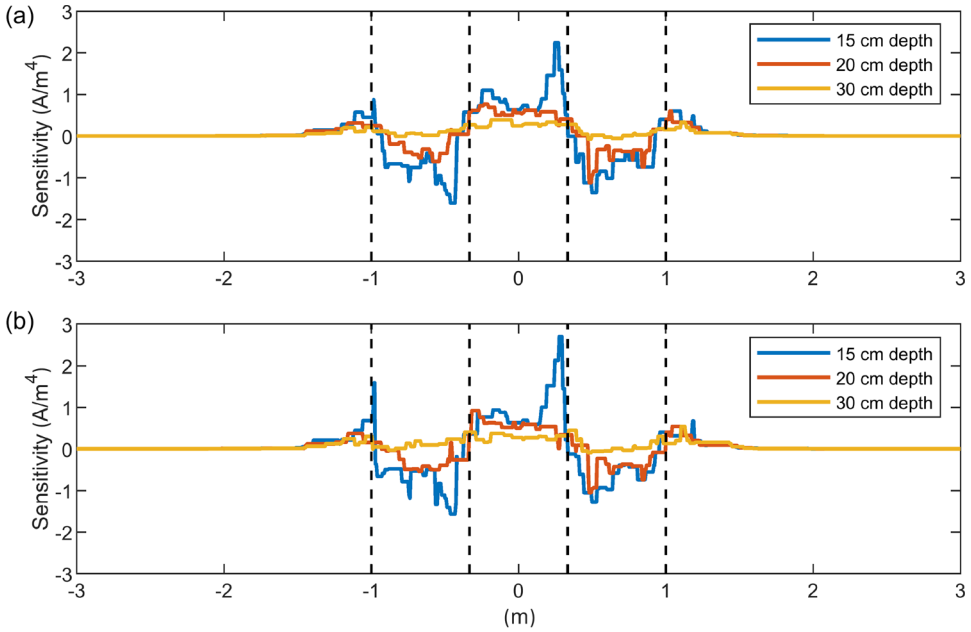


**FIGURE 6** Sensitivity values along horizontal lines at different depths (see arrows in Figure 3) for the Wenner–alpha array. Vertical dashed lines indicate the positions of the electrodes (from right: C1-P1-P2-C2). (a) Analytical values; (b) modelled values.

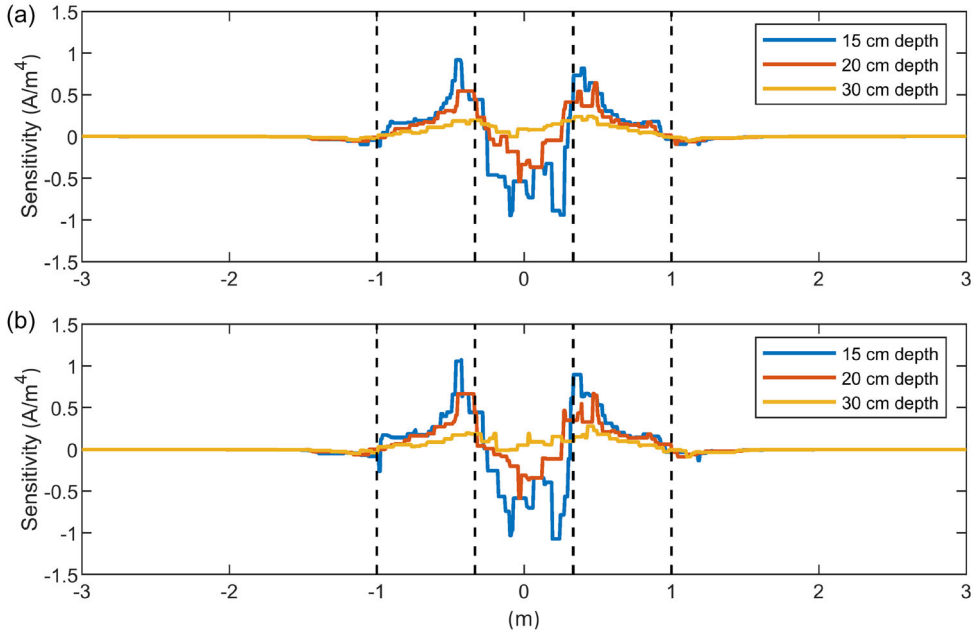


**FIGURE 7** Sensitivity values along horizontal lines at different depths (see arrows in Figure 3) for the dipole–dipole array ($n = 1$). Vertical dashed lines indicate the positions of the electrodes (from right: C2-C1-P1-P2). (a) Analytical values; (b) modelled values.

As expected, the images show that the sensitivity is highest near the electrodes and is very low inside the box-shaped liner when no electrodes are present due to the high resistivity of high-density polyethylene (Figures 4 and 5). To evaluate the sensitivity values in the most relevant area, we extracted three 1 m × 1 m horizontal slices at depths of 0.15 m, 0.6 m and 1.2 m below the liner for all setups. These slices correspond to the area immediately below the liner and to depths roughly equal to half and one distance between the furthest electrodes. Figure 8 presents the slices along with a table that lists, for each slice, the range of volume-normalized sensitivity values and the area-weighted average sensitivity. In the case of

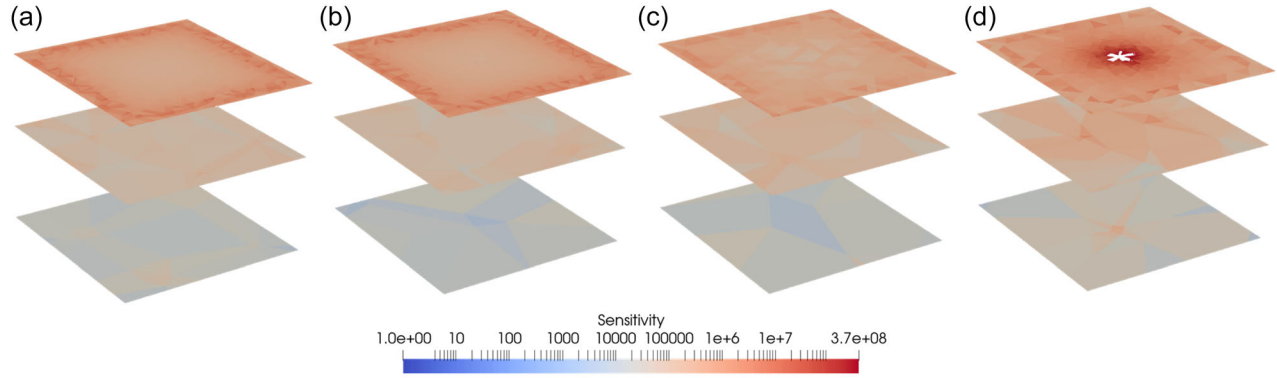


| | CASE 1 - NO HOLE | | CASE 1 - HOLE | | CASE 2 - NO HOLE | | CASE 2 - HOLE | |
|---|---|---|---|---|---|---|---|---|
| | RANGE (A/m$^4$) | AVERAGE (A/m$^4$) | RANGE (A/m$^4$) | AVERAGE (A/m$^4$) | RANGE (A/m$^4$) | AVERAGE (A/m$^4$) | RANGE (A/m$^4$) | AVERAGE (A/m$^4$) |
| **depth = 0.15 m** | (1.60E+05-1.05E+07) | 1.41E+06 | (1.31E+05-9.71E+06) | 1.41E+06 | (5.76E+04-2.84E+06) | 7.89E+05 | (2.12E+05-1.33E+10) | 2.77E+07 |
| **depth = 0.6 m** | (2.21E+04-1.75E+05) | 8.01E+04 | (2.19E+04–1.67E+05) | 7.94E+04 | (6.84E+03–1.89E+05) | 1.08E+05 | (3.52E+04-1.55E+06) | 2.26E+05 |
| **depth = 1.2 m** | (5.39E+03–3.11E+04) | 1.61E+04 | (5.40E+03–3.01E+04) | 1.62E+04 | (3.91E+03–4.40E+04) | 2.21E+04 | (3.23E+03–4.93E+04) | 2.70E+04 |

**FIGURE 8** Sensitivity slices at 0.15 m, 0.6 m and 1.2 m depth for different setups. (a) Forty-eight electrodes outside the box-shaped liner (case 1); (b) same as (a) but with a hole in the liner; (c) 24 electrodes outside the box-shaped liner and 24 electrodes inside (case 2); (d) same as (c) but with a 0.1 m diameter hole in the bottom surface of the liner.

48 electrodes placed outside the liner (case 1), the results do not change significantly if the liner is damaged, as the current is forced to flow between the electrodes without passing through the high-resistivity, box-shaped structure. In contrast, for the case with 24 electrodes inside and 24 electrodes outside (case 2), higher values are recorded at all depths when there is a hole, especially immediately below the liner, where the average and maximum sensitivity values increase by 2 and 4 orders of magnitude, respectively. It is interesting to note that, if there is no hole, the sensitivity values of the shallowest slice are better in case 1. This is reasonable because of the higher number of electrodes outside the box-shaped liner that forces current flow in that region.

Similar considerations can be made by examining the trend of sensitivity values along a vertical line at the centre of the domain (Figure 9). The line goes from the top to the bottom of the domain and passes through the hole when the hole is present. When there is no hole, the sensitivity values are close to zero inside the box-shaped liner only for case 1 (Figure 9a), while they are similar for all tested cases below the liner. In contrast, the tested cases show significant differences when the hole is present. In case 1, sensitivity values increase just inside the liner, whereas in case 2, there is a marked increase in sensitivity across and immediately below the liner (Figure 9b). This trend is also observed when considering the setting with the liner shifted down by 0.05 m (Figure 9c). From these results, the arrangement of electrodes as in case 2 may be promising to detect possible liner damage, even if there is an electrical connection between the landfill and the surrounding media due to improper membrane deployment.

Additional tests performed with smaller holes, with diameters down to 0.02 m, do not provide any new insights. Any hole in the liner can cause a significant increase in the sensitivity values compared to the case without a hole, particularly near the liner. This occurs because significant current densities are concentrated in the area of the hole, as shown by Fumagalli et al. (2024), and the sensitivity increases near any current source (see, e.g., Figure 3).

Regarding the obtained sensitivity values, it is difficult to determine whether they are sufficiently high to provide reliable information about the area beneath the liner. To the best of the authors' knowledge, the scientific literature does not report the minimum sensitivity values required for reliable geoelectrical investigations in the studied domain. Therefore, the following discussion is tentative and non-definitive, based on simplified and arbitrary assumptions.

As mentioned earlier, sensitivity $S$ quantifies how much the electric potential changes in response to variations in resistivity within the considered domain. For a general array of four electrodes, it is defined as a linear combination of the sensitivities of individual pole–pole configurations. Using approximate notation, the sensitivity of the array can be expressed as

$$S = \frac{\Delta\varphi_{\Upsilon,1} - \Delta\varphi_{\Upsilon,2}}{\Delta\rho_{\Upsilon}}, \tag{35}$$

where $\Delta\varphi_{\Upsilon,1}$ and $\Delta\varphi_{\Upsilon,2}$ are the voltage differences [V] measured by the array, respectively, after and before a variation in electrical resistivity $\Delta\rho_{\Upsilon}$ [Ωm] occurs in a specific region of the domain. For a change in resistivity to be detectable, it must cause a potential difference greater than the resolution of the voltmeter. This principle holds ideally from a theoretical standpoint. However, several considerations arise in practical geoelectrical surveys. First, we recall that the measured

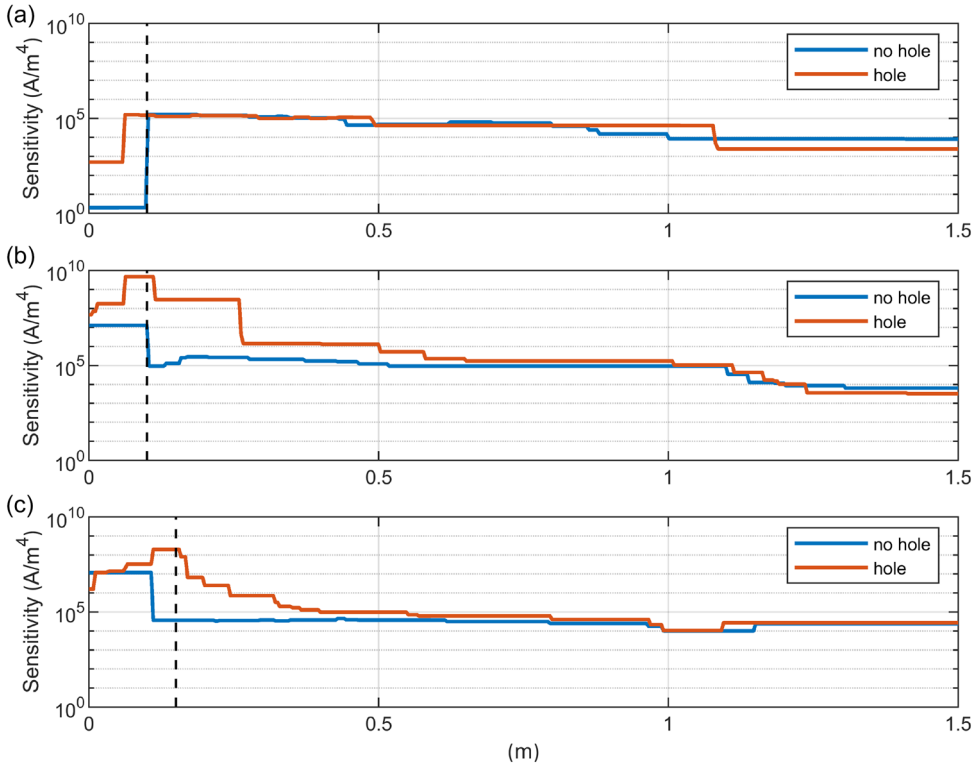


**FIGURE 9** Sensitivity values along a vertical line at the centre of the domain. (a) Forty-eight electrodes outside the box-shaped liner (case 1); (b) 24 electrodes outside the box-shaped liner and 24 electrodes inside (case 2); (c) same as (b) but with liner shifted down by 0.05 m. The vertical dashed line indicates the depth of the bottom surface of the liner.

voltage difference is expressed as

$$\Delta\varphi_{\Upsilon,i} = \frac{\rho_a I}{K}, \tag{36}$$

where $\rho_a$ is the apparent resistivity of the investigated medium, $I$ is the injected current and $K$ is the geometric factor of the array. The first term is not controllable by the user, the second term is generally only partially controllable (e.g., through injection time and the requested voltage at either the current or potential electrodes), while the third term is entirely user-defined. In simple terms, Equation (36) expresses the signal-to-noise ratio (SNR) of the used array and Equation (35) is meaningful only when $\Delta\varphi_{\Upsilon,i}$ exceeds the noise level. To this concern, a minimum potential difference can be established as a reliability threshold. For example, with the IRIS Syscal Pro georesistivimeter, the minimum reception voltage when the device operates in 'save-energy' mode, namely 15 mV (compared to the voltmeter resolution of 1 $\mu$V) can be set. With an arbitrary yet conservative approach, the same threshold can be applied to the variation in the measured potential difference in Equation (35). Additionally, a target $\Delta\rho_\Upsilon$, representing the desired resistivity resolution of the geoelectrical survey, must be defined in Equation (35). Using a conservative (and demanding) approach, a value as low as 1 Ωm can be adopted. With the aforementioned values, Equation (35) yields

$$S = \frac{\Delta\varphi_{\Upsilon,1} - \Delta\varphi_{\Upsilon,2}}{\Delta\rho_\Upsilon} \geq \frac{1.5\times10^{-3}\ \text{V}}{1\ \Omega\text{m}} = 1.5\times\ 10^{-3}\text{A m}^{-1} \tag{37}$$

Given that our synthetic tests involve 48 deployed electrodes and approximately $6\times10^5$ configurations, the global sensitivity in each area (i.e., cell) of the considered domain is expressed as

$$S \geq 6\times\ 10^5\times\ 1.5\times10^{-3}\text{A m}^{-1} = 9\times\ 10^2\text{A m}^{-1}. \tag{38}$$

However, some configurations may not significantly contribute to increasing the global sensitivity (e.g., due to excessively low SNR), meaning the global sensitivity calculated above is likely an overestimation of the actual sensitivity.

It is also important to note that the obtained sensitivity values are normalized by the volume of each mesh cell. This normalization is necessary because larger cell volumes result in higher sensitivity values. Given that the characteristic length of the liner mesh is 0.05 m and the 3D elements of the mesh conform to the liner, we can assume that the 3D cells near the liner are regular tetrahedra with a volume of approximately $1.5\times10^{-5}$ m$^3$. With this, Equation (38)

becomes

$$S \geq \frac{9 \times 10^{2}\ \mathrm{A\ m^{-1}}}{1.5 \times 10^{-5}\ \mathrm{m^{3}}} = 6 \times 10^{7}\ \mathrm{A\ m^{-4}}. \quad (39)$$

Finally, and most importantly, the modelled sensitivity values were obtained using an injected current of 1 A, which significantly impacts the results since sensitivity depends linearly on the injected current (see the Equidimensional Sensitivity section). As mentioned earlier, the injected current is only partially controllable and may vary depending on the resistivities within the domain. However, injected currents of approximately 1 A are common in geoelectrical field surveys and are easily managed by commercial georesistivimeters (e.g., IRIS Syscal Pro Switch).

For these reasons, the sensitivity threshold in Equation (39) should be regarded as a simplified and conservative estimate. The average sensitivity values obtained from depth slices immediately below the liner are approximately an order of magnitude lower than the threshold for nearly all tested cases, except for case 2 with the hole, where the average sensitivity value is of the same order of magnitude (Figure 8). Similar observations apply to peak sensitivity values near the liner. These values exceed the threshold when a hole is present and electrodes are placed both inside and outside the liner. In contrast, they fall below the threshold when the liner is undamaged (Figure 9).

Given that the minimum sensitivity estimate was derived using a series of simplifying but conservative assumptions, we believe that direct current (DC) surveys have the potential to detect liner damage with electrode spreads positioned along the liner perimeter, both outside and inside the landfill. However, laboratory testing on similar setups is essential to validate our modelling results.

To gain insight into the electrode configurations that maximize sensitivity in landfill field investigations, we focused on the most promising spread deployment, specifically case 2. We analysed the sensitivity of cells within a volume directly below the liner, defined as a square prism with dimensions 1 m × 1 m × 0.1 m. For each configuration tested, we computed the L1 norm by adding the absolute values of the sensitivity in each cell within the defined volume. The configurations were then ranked in descending order according to their L1 norm. This analysis was conducted for both the setups with and without a hole in the bottom surface of the liner. Given that liner conditions are not known in field surveys, we identified the intersection of the top 1000 configurations (ranked by the L1 norm) of both setups. The results indicate that the configurations with the highest sensitivity are quadrupoles in which both the current and voltage dipoles have one electrode inside the liner and one electrode outside. Furthermore, the most effective quadrupoles feature a 2D arrangement of the electrodes (i.e., the four electrodes are not along a line).

## CONCLUSIONS

We have presented and validated a new mixed-dimensional code to accurately compute the sensitivity of direct current investigations of municipal solid waste landfills (MSWLFs), where a highly resistive membrane is typically placed underneath the waste mass to avoid subsurface contamination concerns. The mixed-dimensional framework is useful to tackle the computational costs and ill-posedness of the geoelectrical inverse problem by modelling the electrodes and, most importantly, the resistive liner as one- and two-dimensional (2D) elements, respectively. Besides some technical implementation aspects described before, the code uses Green's functions to speed up the computation of both voltage difference and the sensitivity for each electrode configuration.

According to preliminary modelling of downscaled and simplified landfill settings, acquisitions with all electrodes placed outside the perimeter edges of the box-shaped liner may not be able to detect a hole in the most challenging location, that is, at the centre of the bottom surface of the liner. In contrast, acquisitions with the same number of electrodes deployed along the perimeter of the liner, but placed both inside and outside the landfill, may detect potential damage to the liner as sensitivity increases near the damaged area. No significant improvement has been observed when the electrodes inside the landfill are arranged in a grid pattern. Therefore, linearly arranged electrodes on both sides of the liner should be preferred because their deployment is logistically easier, particularly in the presence of steep and uneven landfill topography. In addition, electrodes running across the landfill topography may be too far from the underlying liner, causing issues with resolution and penetration depth. Furthermore, the topography may affect the final results if not properly taken into account. Electrodes arranged linearly along both sides of the perimeter edges of the liner can also be used to check the electrical insulation of the landfill relative to the surrounding medium by measuring the electrical resistance between adjacent electrode pairs.

Our simulations show that the results do not differ significantly for holes with diameters ranging from approximately one electrode spacing to one-sixth of the electrode spacing. Even with relatively small damage, the sensitivity increases by 2 to 3 orders of magnitude, which is promising for landfill-monitoring purposes.

The above considerations still apply when the liner is not in contact with the top of the domain. This setting is common in the field and can simulate electrical connections between the landfill and the surrounding media due to downshifts of the liner or conductive materials covering its perimeter edges.

The modelled sensitivity values beneath the liner are close to a minimum sensitivity threshold derived from simplified and arbitrary assumptions. We believe that DC surveys have the potential to detect liner damage using electrode spreads

positioned along the liner perimeter, both inside and outside the landfill. However, down-scaled laboratory tests will be necessary to validate the modelling results and confirm whether the computed sensitivity values are high enough to reliably detect liner damage.

In addition, an appropriate number of measurements will need to be evaluated to ensure sensitivity levels that meet the survey objectives with a reasonable field effort. Our code to compute the sensitivity can obviously be used to select the best configuration and to design electrical acquisitions with the aim of achieving both the appropriate investigation depth (e.g., where the liner is located) and spatial resolution. In our tests, we observe that when electrodes are deployed along the perimeter of the liner, both inside and outside the landfill, the configurations with the highest sensitivity directly beneath the liner are quadrupoles with a 2D electrode arrangement (i.e., the four electrodes are not aligned linearly). In these configurations, both the current and voltage dipoles have one electrode inside the box-shaped liner and one outside.

To improve sensitivity at depth, at the expense of higher costs and more complex data processing, cross-borehole electrical resistivity tomography imaging can also be considered.

Finally, although we have noted that sensitivity affects the resolution and penetration depth of geoelectrical surveys and depends on factors such as physical approximations in the forward model, survey geometry and resistivity distribution, real scenarios also require consideration of measurement errors, data signal-to-noise ratio, as well as parameterization and regularization used in the inversion (Binley & Kemna, 2005).

## ACKNOWLEDGEMENTS

The authors thank Prof. Luigi Zanzi for fruitful discussions. The present research is part of the activities of "Dipartimento di Eccellenza 2023-2027", Italian Minister of University and Research (MUR), grant Dipartimento di Eccellenza 2023-2027.

Open access publishing facilitated by Politecnico di Milano, as part of the Wiley - CRUI-CARE agreement.

## DATA AVAILABILITY STATEMENT

The data that support the findings of this study are available from the corresponding author upon reasonable request.

## ORCID

*Lorenzo Panzeri* https://orcid.org/0009-0002-5722-2598

## REFERENCES

Aavatsmark, I. (2002) An introduction to multipoint flux approximations for quadrilateral grids. *Computational Geosciences*, 6, 405–432.

Aavatsmark, I. (2007) Multipoint flux approximation methods for quadrilateral grids. In *The 9th International Forum on Reservoir Simulation, Abu Dhabi, United Arab Emirates*.

Aguzzoli, A., Hojat, A., Zanzi, L. & Arosio, D. (2020) Two dimensional ERT simulations to check the integrity of geomembranes at the base of landfillbodies. In *NSG2020 26th European Meeting of Environmental and Engineering Geophysics*, volume 2020. Houten, the Netherlands: European Association of Geoscientists & Engineers, 1-5.

Aldridge, D. & Oldenburg, D. (1989) Direct current electric potential field associated with two spherical conductors in a whole-space 1. *Geophysical Prospecting*, 37(3), 311–330.

Bernstone, C., Dahlin, T., Ohlsson, T. & Hogland, H. (2000) Dc-resistivity mapping of internal landfill structures: two pre-excavation surveys. *Environmental Geology*, 39, 360–371.

Binley, A. & Daily, W. (2003) The performance of electrical methods for assessing the integrity of geomembrane liners in landfill caps and waste storage ponds. *Journal of Environmental and Engineering Geophysics*, 8(4), 227–237.

Binley, A. & Kemna, A. (2005) DC resistivity and induced polarization methods. In: Rubin, Y., Hubbard, S.S. (eds) *Hydrogeophysics*. Water Science and Technology Library, vol 50, 129-156. Springer, Dordrecht.

Dahlin, T., Rosqvist, H. & Leroux, V. (2010) Resistivity-IP mapping for landfill applications. *First Break*, 28(8), 101–105.

Day-Lewis, F.D., Singha, K. & Binley, A.M. (2005) Applying petrophysical models to radar travel time and electricalresistivity tomograms: resolution-dependent limitations. *Journal of Geophysical Research*, 110, B08206.

De Carlo, L., Perri, M.T., Caputo, M.C., Deiana, R., Vurro, M. & Cassiani, G. (2013) Characterization of a dismissed landfill via electrical resistivity tomography and mise-á-la-masse method. *Journal of Applied Geophysics*, 98, 1–10.

De Donno, G. & Cardarelli, E. (2017) Tomographic inversion of time-domain resistivity and chargeability data for the investigation of landfills using a priori information. *Waste Management*, 59, 302–315.

Edwards, L.S. (1977) A modified pseudosection for resistivity and induced-polarization. *Geophysics*, 42(5), 939–1087.

European Commission (2015) Closing the loop-an EU action plan for the circular economy. Communication from the Commission to the European Parliament, the Council, the European Economic and Social Committee and the Committee of the Regions. Technical report, Brussels: European Commission.

Frangos, W. (1997) Electrical detection of leaks in lined waste disposal ponds. *Geophysics*, 62(6), 1737–1744.

Fumagalli, A., Panzeri, L., Formaggia, L., Scotti, A. & Arosio, D. (2024) A mixed-dimensional model for direct current simulations in the presence of a thin high-resistivity liner. *International Journal for Numerical Methods in Engineering*, 125(6), e7407.

Geuzaine, C. & Remacle, J.-F. (2009) Gmsh: A 3-D finite element mesh generator with built-in pre- and post-processing facilities. *International Journal for Numerical Methods in Engineering*, 79(11), 1309–1331.

Giroux, L. (2014) State of waste management in Canada. Giroux Environmental Consulting. Technical report, Canadian Council of Ministers of the Environment, Kanata, Ontario, Canada.

Jones, P. T., et al,. (2013) Enhanced landfill mining in view of multiple resource recovery: a critical review. *Journal of Cleaner Production*, 55, 45–55.

Li, X.S. (2005) An overview of SuperLU: Algorithms, implementation, and user interface. *Transactions on Mathematical Software*, 31(3), 302–325.

Ling, C., Revil, A., Qi, Y., Abdulsamad, F., Shi, P., Nicaise, S. & Peyras, L. (2019) Application of the mise-à-la-masse method to detect the bottom leakage of water reservoirs. *Engineering Geology*, 261, 105272.

Loke, M. & Barker, R. (1995) Least-squares deconvolution of apparent resistivity pseudosections. *Geophysics*, 60(6), 1682–1690.

Loke, M.H. (2022) Tutorial: 2-D and 3-D electrical imaging surveys. Course notes. Accessible at https://www.geotomosoft.com/

Mcgillivray, P.R. & Oldenburg, D. (1990) Methods for calculating Fréchet derivatives and sensitivities for the non-linear inverse problem: a comparative study. *Geophysical Prospecting*, 38(5), 499–524.

Nanda, S. & Berruti, F. (2021) Municipal solid waste management and landfilling technologies: a review. *Environmental Chemistry Letters*, 19, 1433–1456.

Panzeri, L., Fumagalli, A., Aguzzoli, A., Zanzi, L., Longoni, L., Papini, M., & Arosio, D. (2023) Lab and modelling DC resistivity tests to analyse the response of a high resistivity liner. In *5th Asia Pacific Meeting on Near Surface Geoscience & Engineering*, volume 2023. Houten, the Netherlands: European Association of Geoscientists & Engineers, pp. 1–5.

Panzeri, L., Fumagalli, A., Zanzi, L., Longoni, L., Papini, M. & Arosio, D. (2023) Validation of a mixed-dimensional code for the analysis of highly resistive liners in landfills. In *NSG2023 29th European Meeting of Environmental and Engineering Geophysics*, volume 2023. Houten, the Netherlands: European Association of Geoscientists & Engineers, pp. 1–5.

Park, S.K. & Van, G.P. (1991) Inversion of pole-pole data for 3-D resistivity structure beneath arrays of electrodes. *Geophysics*, 56(7), 951–960.

Peters, A. (2016) These maps show how many landfills there are in the U.S. (accessed 20 July 2024). Accessible at https://www.fastcompany.com/3062853/these-maps-show-how-much-of-the-us-is-covered-in-landfills

Raviart, P.-A. & Thomas, J.-M. (1977) A mixed finite element method for second order elliptic problems. *Lecture Notes in Mathematics*, 606, 292–315.

Rücker, C., Günther, T. & Wagner, F.M. (2017) pygimli: an open-source library for modelling and inversion in geophysics. *Computers & Geosciences*, 109, 106–123.

Salsa, S. (2016) *Partial differential equations in action. From modelling to theory*, volume 99 of *La Matematica per il 3+2*. Cham: Springer International Publishing.

Sheriff, R.E., Telford, W.M. & Geldart, L.P. (1990) *Applied geophysics* (2nd ed.). Cambridge, UK: Cambridge University Press.

Tsourlos, P., Vargemezis, G., Fikos, I. & Tsokas, G. (2014) DC geoelectrical methods applied to landfill investigation: case studies from Greece. *First Break*, 32(8), 81–89.

Wagner, T.P. & Raymond, T. (2015) Landfill mining: case study of a successful metals recovery project. *Waste Management*, 45, 448–457.

**How to cite this article:** Panzeri, L., Fumagalli, A., Longoni, L., Papini, M. & Arosio, D. (2025) Sensitivity analysis with a 3D mixed-dimensional code for direct current geoelectrical investigations of landfills: synthetic tests. *Geophysical Prospecting*, 1–16. https://doi.org/10.1111/1365-2478.70006